MIT Open Access Articles

An in situ synchrotron X-ray study of reverse austenitic transformation in a metastable FeMnCo alloy

Check for updates

An in situ synchrotron X-ray study of reverse austenitic transformation in a metastable FeMnCo alloy

Shaolou Wei[1] , Jiyun Kang[1], Cemal Cem Tasan[1,a)]

[1] Department of Materials Science and Engineering, Massachusetts Institute of Technology, Cambridge, MA 02139, USA
a) Address all correspondence to this author. e-mail: tasan@mit.edu

This study concerns reverse austenitic transformation of plastic strain-induced hexagonal close-packed martensite. With the aid of in situ synchrotron X-ray diffractometry, the kinetic features of the transformation and the defect content evolution in a metastable $(Fe_{60}Mn_{40})_{85}Co_{15}$ alloy are quantitatively examined using 5, 20, and 100 °C/min heating rates. It is found that the reverse austenitic transformation can be activated below 200 °C and completes within a short time scale. Through a Kissinger-style kinetic analysis, the activation energy of the reverse austenitic transformation is determined as 171.38 kJ/mol, confirming its displacive nature. Although exponential attenuation is observed in both stacking fault probability and dislocation density upon the initiation of the transformation, the resulting microstructure (single-phase face-centered cubic structure) remains highly defected, exhibiting high Vickers hardness, but still preserving somewhat strain hardenability. Atomistic mechanisms for the reverse austenitic transformation are further conceived according to the crystallographic theory of martensitic transformation.

Introduction

Displacive phase transformations driven by mechanical load are a class of beneficial mechanisms in promoting the load-bearing performance of metallic alloys [1–3]. Among them, plastic strain-induced martensitic transformation alone has led to significant research attention [4, 5]. Apart from the appreciable efforts attempting to maximize its mechanical benefits of strain hardenability improvement [6–8], the underlying atomistic mechanisms [9, 10], as well as the crystallographic nature of the transformation strain [11], have also triggered increasing theoretical interest. As a result, successful alloy design concepts exploiting strain-induced martensitic transformation are numerous: transformation-induced plasticity (TRIP) steels [12], biomedical Co-based alloys [13], and the quick-emerging metastable high- and medium-entropy alloys [14].

Unlike the considerable focus on the strain-induced martensitic transformation, its mechanistic counterpart, reverse austenitic transformation driven by heating, appears rather less explored, and the potential in guiding application-worthy microstructural design remains unclear. However, technological advancement in rapid thermal treatment approaches has greatly facilitated the exploration of applying this phase transformation

pathway to access better mechanical and/or functional properties [15, 16]. Historical records can be dated back to the 1970s [17], when Gridnev et al. reported the significant strength-ductility synergy enhancement through rapid induction heating of martensitic microstructures. In the past two decades, the progress in high-energy laser beam annealing has opened an intriguing pathway to extend the benefits of reverse austenitic transformation. Numerous investigations [18–23] have showcased the improvements in strength, strain hardenability, and even formability through local rapid annealing to activate such a transformation. These engineering merits further call for more dedicated study of the underlying transformation mechanisms.

The reverse austenitic transformation can exhibit great mechanistic diversity depending on the alloy chemistry and the applied heating rate. The transformation pathways can either be diffusive or displacive and the general observations are outlined as follows, based on the literature of Fe–Mn-type metastable alloys [24–29]. In body-centered tetragonal (BCT) martensite, where the Mn content is typically 5–12 wt.%, the reverse austenitic transformation is diffusive at slower heating rates (roughly below 10 °C/s) but turns into displacive as the heating rate increases. In hexagonal close-packed (HCP) martensite, on the other hand, where the

Mn content is in the range of 15–30 wt.%, the reverse austenitic transformation is mainly displacive, regardless of the applied heating rate. The present work focuses on the latter. Holding a triplex Burgers orientation relationship with the parent face-centered cubic (FCC) austenite [11], i.e. $\{\bar{1}11\}_{FCC}//\{0001\}_{HCP}$, $\langle 110\rangle_{FCC}//\langle 11\bar{2}0\rangle_{HCP}$, and $\langle \bar{1}12\rangle_{FCC}//\langle 1\bar{1}00\rangle_{HCP}$, reverse austenitic transformation of the HCP-martensite has attracted vibrant attention. Systematic studies performed on cold-rolled Fe–Mn–C metastable alloys [29–32] confirmed the relatively low onset temperature (~ 200 °C) of the transformation and the pronounced increase in S-type texture component as a result of the transformation. Several other studies have been subsequently accomplished [33–35], aiming to modulate the reverse transformation kinetics by controlling the annealing temperature or isothermal holding time, and evident mechanical property improvements can be feasibly achieved. More recent literature also reflects the trend of exploiting ab initio simulation methods to quantitatively uncover the detailed thermodynamics embedded behind such a transformation [36, 37].

Although salient success has been achieved in the foregoing experimental work investigating the kinetics of the transformation through dilatometer, its limitations largely exist in the deficiency in quantifying defect evolution and detailed lattice structural change in a spatially-resolved manner. In situ synchrotron X-ray diffractometry, when coupled with controlled heating rate testing instrument, might overcome these dilemmas to some extent [38, 39]. The advantages of such experimental methods lie in their capability in capturing lattice strain variation, phase constitution change, and stacking fault fraction evolution in a statistically representative volume of a material during any heating process. These quantities are especially meaningful to deepen the understanding of the displacive reverse austenitic transformation mechanisms.

The present work investigates the thermally-driven reverse austenitic transformation in a metastable $(Fe_{60}Mn_{40})_{85}Co_{15}$ alloy. Through in situ synchrotron X-ray diffraction experiments under three different heating rates (5, 20, and 100 °C/min), the kinetic features of the transformation, the defect characteristics and the evolution trends in their contents are quantitatively examined. A plausible atomistic pathway for the displacive reverse transformation is conceived based on the crystallographic theory. Mechanical properties including Vickers hardness and strain hardenability are further evaluated to explore the potential microstructural design strategies.

Results

Initial microstructure and diffraction profile evolution during heating

Microstructures of the $(Fe_{60}Mn_{40})_{85}Co_{15}$ alloy at fully recrystallized and cold-rolled conditions are revealed in Fig. 1(a and

b). The fully recrystallized microstructure [Fig. 1(a)], although achieved through rapid thermal quenching from 900 °C, only consists of FCC phase, as cross-validated by the synchrotron X-ray diffraction profile in Fig. 1(c). The application of cold work on the fully crystallized specimen activates plastic strain-induced martensitic transformation in this alloy. The fact that the martensitic transformation is driven by plastic strain has been verified in an earlier study [40]. For completeness, in situ synchrotron tensile results are provided in Supplementary Fig. S1, in which noticeable HCP-martensite peaks can only be detected after the inception of plastic deformation. As seen in Fig. 1(b) and the magnified inset, an extensive amount of HCP-martensite nucleates after 50 % cold rolling. By Rietveld refining the corresponding diffraction profile [Fig. 1(c)], the HCP-martensite fraction is determined as 0.619. No BCT martensite is detected at the resolution limits of backscattering electron (BSE)/electron channeling contrast imaging (ECCI) or synchrotron X-ray diffraction. Comparing the diffraction profiles obtained at these two conditions, three evident differences can be phenomenologically observed after cold working: (1) the appearance of HCP diffraction peaks; (2) the shifts of FCC peak positions; and (3) the broadening of FCC peaks. The physical revelation of these phenomena will be further explored in the next two sections.

To assess the reverse austenitic transformation in this metastable alloy, continuous heating experiments were carried out under in situ synchrotron X-ray diffraction. The present work selected three heating rates (5, 20, and 100 °C/min) which cross an order of magnitude for the kinetic study. The experimental setup is sketched in Fig. 2, and its actual configuration is provided in Supplementary Fig. S2. It should be noted that because diffractograms are recorded in an in-operando manner during continuous heating, the temperature mentioned hereafter is an arithmetic average of the temperature values when the detector shutter is open and close as shown in Eq. (1) (also see Supplementary Fig. S3 for more details):

$$T = \frac{1}{2}\left(T_{shutter\ open} + T_{shutter\ close}\right) \qquad (1)$$

Figure 3 exemplifies the evolutionary properties of the diffraction profiles with respect to temperature increase obtained from the the 5 °C/min heating rate experiment. Two-dimensional diffractograms selected at four representative temperatures confirm the onset of the thermally-driven reverse austenitic transformation [Fig. 3(a1–4)]. At an ambient temperature of 25 °C, the diffractogram consists of both FCC and HCP reflection groups [Fig. 3(a1)]. The $\{10\bar{1}0\}_{HCP}$, the $\{10\bar{1}1\}_{HCP}$, and the $\{11\bar{2}0\}_{HCP}$ rings are marked with red arrows as a guide to the eye. As the temperature increases to 217 °C, discernable intensity reduction can be seen from the $\{11\bar{2}0\}_{HCP}$ reflection, indicating the thermal instability of the HCP-martensite [Fig. 3(a2)]. At such a temperature, changes in the $\{10\bar{1}0\}_{HCP}$ and the $\{10\bar{1}1\}_{HCP}$ reflections
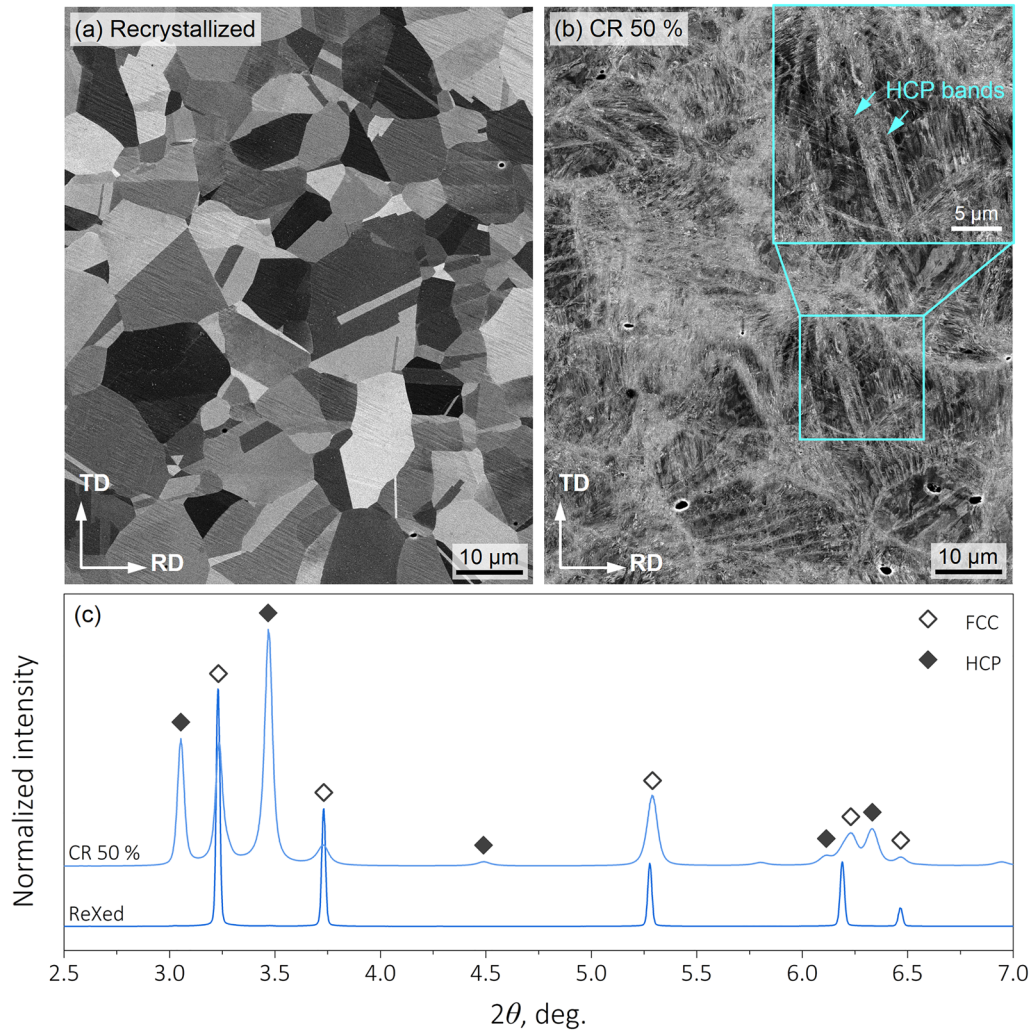
Figure 1: Plastic strain-induced martensitic transformation in the (Fe$_{60}$Mn$_{40}$)$_{85}$Co$_{15}$ alloy: (a) fully recrystallized microstructure with equiaxed grain morphology (grain size ~25 μm); (b) BSE image of the 50 % cold-rolled microstructure. The inset is an ECCI micrograph showing the HCP-martensite bands; **c** integrated synchrotron X-ray diffraction profiles for the two microstructures. Abbreviations in the figure: rolling direction (RD); transverse direction (TD); recrystallized (ReXed).

remain visually subtle. Upon further heating, these three diffraction rings all reveal noticeable decrease in intensities at 321 °C, suggesting the evident progression of the HCP-martensite reverse transformation [Fig. 3(a3)]. As the temperature reaches 500 °C, HCP diffraction signals can no longer be detected, and the diffractogram fully consists of FCC reflection groups [Fig. 3(a4)]. These observations underpin the relatively low stability of the plastic strain-induced martensite against heating, in which reverse austenitic transformation completes below 500 °C.

To fully resolve the evolutionary features of the diffraction profiles, the two-dimensional diffractograms were integrated over the entire 360° azimuthal angle and the corresponding intensity information was extracted for color interpolation. Figure 3(b1) shows the integrated diffraction profile evolution as a function of temperature (heating curve shown in Fig. 3(b2)).

Apart from the phase transformation features mentioned above, a few other important phenomena should also be mentioned, followed by quantitative analyses and discussion in "Kinetics of reverse austenitic transformation" and "Defect content evolution during reverse austenitic transformation" sections: (1) all diffraction peak positions tend to shift to the lower 2θ region as temperature increases; (2) the $\{111\}_{FCC}$ reflection group reveals the highest intensity increase upon heating; and (3) peak broadening features tend to reduce in almost all reflection groups (except $\{200\}_{FCC}$) as heating proceeds.

Kinetics of reverse austenitic transformation

The kinetic features of the reverse austenitic transformation are analyzed here with a primary focus on phase fraction evolution. For the clarity of quantification, the FCC-phase fraction is firstly
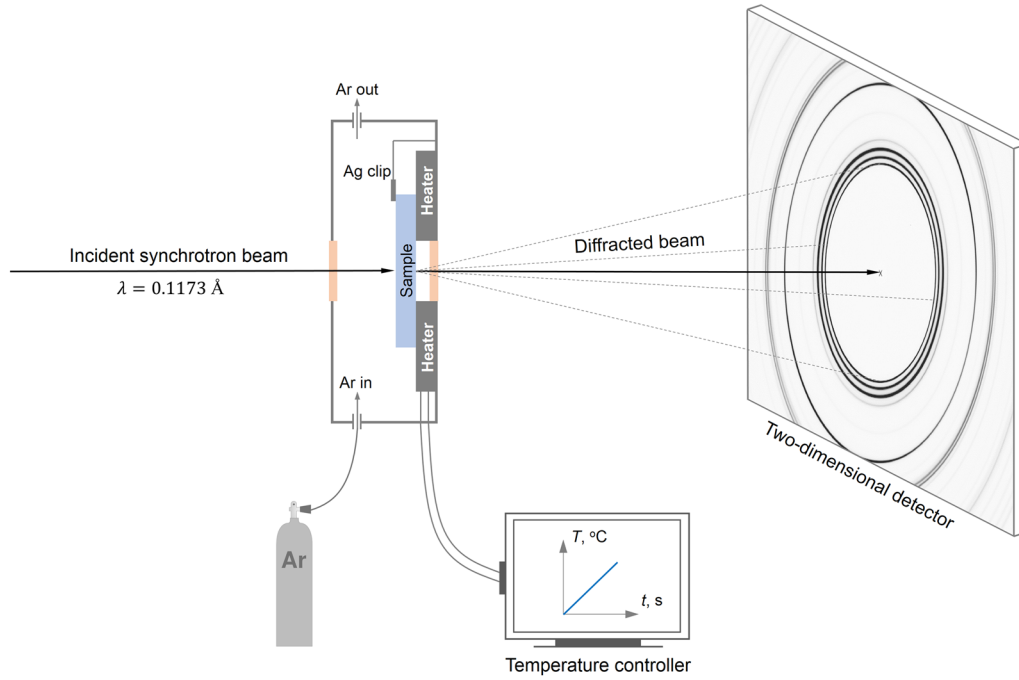
Figure 2: Schematic of the experimental setup for in situ synchrotron X-ray measurements during continuous heating: A continuous flow of Ar gas is supplied throughout the entire measurement period to minimize oxidation. The sample is compressed onto the heater by a silver clip, which also ensures temperature homogeneity.
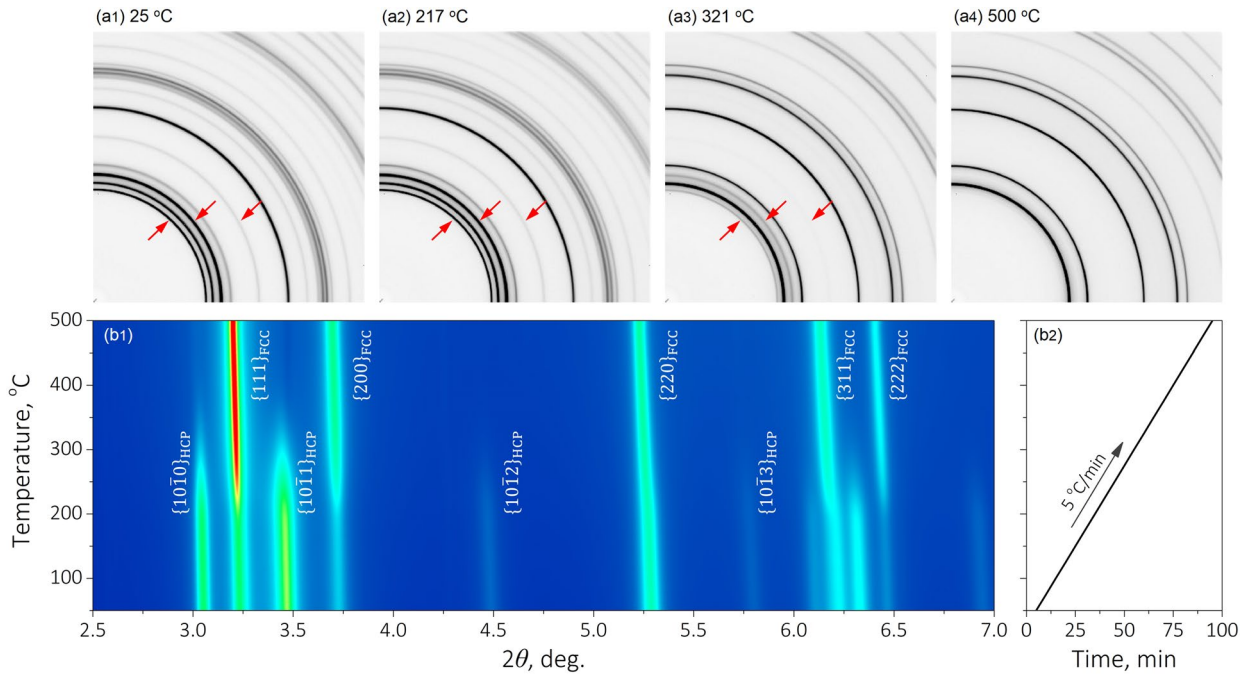
Figure 3: In situ synchrotron X-ray characterization of reverse austenitic transformation: (a1–a4) snapshots of two-dimensional diffractograms acquired at the increasing temperatures of 25, 217, 321, and 500 °C; (b1) integrated diffraction profiles presented as a function of continuous temperature increase. Color interpolation exploits the corresponding intensity data of individual diffraction peaks; (b2) temperature change corresponds to (b1).

normalized in a sense to more evidently reveal its evolutionary trend:

$$\beta = \frac{f_{FCC}^T - f_{FCC}^o}{1 - f_{FCC}^o} = \frac{f_{FCC}^T - f_{FCC}^o}{f_{HCP}^o} \quad (2)$$

In Eq. (2), f_{HCP}^o and f_{FCC}^o are the HCP-martensite and the FCC-phase fractions at the un-heated condition (i.e. after 50 % cold rolling). f_{FCC}^T denotes the FCC-phase fraction measured by the Rietveld refinement at a temperature T. As a result, at the starting point of the heating experiment, the β factor is 0, signifying that no reverse austenitic transformation has taken place. Upon the progression of the transformation, the β factor increases and eventually reaches 1 when the transformation is complete, since $(f_{FCC}^T - f_{FCC}^o)_{max} = 1 - f_{FCC}^o = f_{HCP}^o$.

The experimentally measured β factors as a function of temperature under three heating rates are summarized in Fig. 4(a1–a3). These datum points are further assessed using

Boltzmann's sigmoidal model (see the solid lines in these figures):

$$\beta = 1 - \left[1 + \exp\left(\frac{T - T_c}{dT}\right)\right]^{-1} \quad (3)$$

In Eq. (3), β is the normalized FCC-phase fraction that quantifies the extent of the reverse austenitic transformation as a function of temperature. T_c and dT are fitting parameters, representing the center temperature for the transformation (i.e. the temperature where β=0.5) and the slope factor. From a physical perspective, dT describes the constant portion in T that controls the increase in β. A higher dT implies the transformation tends to span over a broader temperature range. This slope factor was further adopted to determine the austenite start (A_s) and finish (A_f) temperatures. Table 1 summarizes the heating rate dependence of the aforementioned parameters.

The plastic strain-induced HCP-martensite becomes thermally unstable at ~150 °C under all three heating conditions
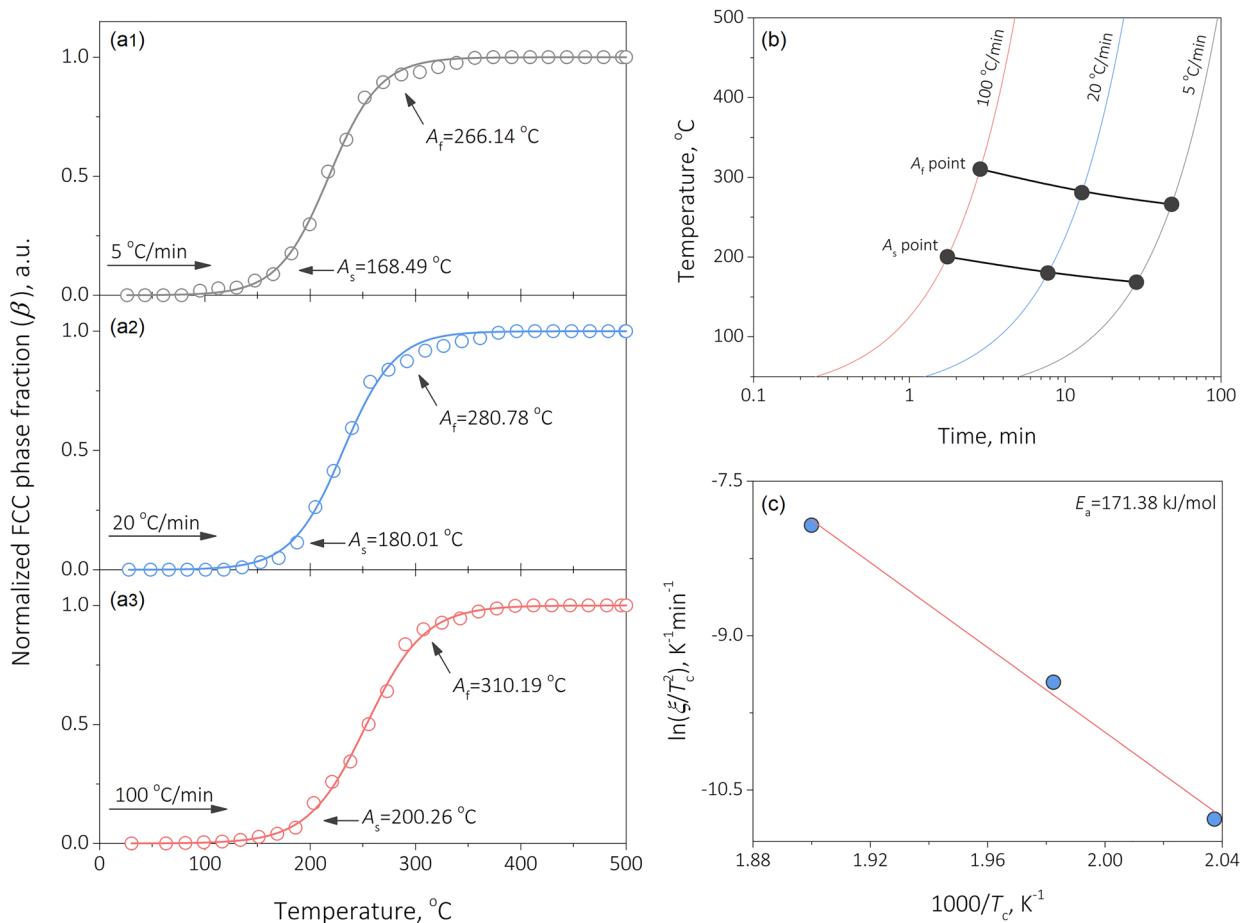

Figure 4: Kinetics of reverse austenitic transformation: (a1–a3) normalized FCC-phase fraction evolution with respect to increasing temperature tested under three different heating rates; (b) A_s and A_f temperatures denoted on the continuous heating rate plots; (c) Kissinger-style kinetic analysis of the activation energy.

TABLE 1: Heating rate dependence of the kinetic factors and the austenite start and finish temperatures.

Heating rate, °C/min	T_c, °C	dT, °C	A_s, °C	A_f, °C
5	217.84	24.03	168.49	266.14
20	231.43	24.58	180.01	280.78
100	253.52	27.55	200.26	310.19

[Fig. 4(a1–a3)]. Such a trend is consistent with the earlier report in the literature regarding Fe–Mn-type metastable alloys [41–43]. Further assessments of Fig. 4(a1–a3 and b) conclude that although the reverse austenitic transformation completes within a relatively narrow temperature range (roughly 150–300 °C), heating rate dependency still moderately exists. Both the A_s and the A_f points show approximately 30 °C increase as the heating rate increases from 5 to 100 °C/min. The entire transformation also tends to span over a slightly wider temperature range, as featured by both the increase in dT as well as the difference between A_s and A_f [Fig. 4(b)].

The good agreement observed between the experimental data and the Boltzmann sigmoidal model physically indicates that the reverse austenitic transformation reveals a maximum rate (i.e. $\frac{\partial^2}{\partial T^2}\beta(T) = 0$) in each constant heating rate measurement. This feature rationalizes a Kissinger-style analysis [44, 45] to further quantify the activation energy for the transformation. In the Kissinger-style analysis, an Arrhenius-type dependency can be derived for the maximum rate temperature [44]:

$$\ln(\frac{\xi}{T_c^2}) = -\frac{E_a}{R T_c} + \ln\left(\frac{AR}{E_a}\right) \qquad (4)$$

In Eq. (4), ξ is the constant heating rate adopted in the experiment. For the present work, ξ takes the values of 5, 20, and 100 K/min. E_a, T_c, A, and R respectively denote the activation energy, the maximum rate temperature (note that the unit is Kelvin), the fitting constant, and the gas constant (8.314 J·mol^{-1}·K^{-1}). Figure 4(c) reveals a $\ln(\frac{\xi}{T_c^2})$ versus $\frac{1000}{T_c}$ plot calculated from the experimental data. A desirable linearity is present and the activation energy is determined as 171.38 kJ/mol. Such an activation energy, although slightly higher than typical values measured from thermoelastic martensite [46, 47], is much lower than the energy barrier of bulk diffusion-driven transformation in ferrous alloys [48, 49]. Note that this energy should not be confused with the thermodynamic driving force for phase transformation. The latter instead describes the energy difference between the reactant and the product and cannot be assessed by the Kissinger-style analysis. The moderate heating rate dependence, the low A_s temperature, and the low activation energy all support the fact that the reverse austenitic transformation in the present $(Fe_{60}Mn_{40})_{85}Co_{15}$ alloy is achieved through a displacive pathway. A more in-depth discussion on the underlying atomistic processes and microstructural consequences is provided in "The displacive nature of reverse austenitic transformation" section.

Defect content evolution during reverse austenitic transformation

To shed a bit more quantitative light on the crystalline defects involved in the reverse austenitic transformation, the integrated diffraction profiles [see Fig. 1(c) or Fig. 3(b1)] were firstly Gaussian fitted to determine the FCC peak positions and to calculate the corresponding d-spacings. The peak shifting phenomena mentioned in "Initial microstructure and diffraction profile evolution during heating" section are next quantified by the apparent lattice strain [50]:

$$d_{hkl}^{app.} = \frac{d_{hkl}^T - d_{hkl}^0}{d_{hkl}^0} \qquad (5)$$

In Eq. (5), d_{hkl}^o and d_{hkl}^T denote the d-spacing of the $\{hkl\}_{FCC}$ reflection group at the fully recrystallized state and at a temperature of T during heating. Figure 5 shows the apparent lattice strain evolution of a total of five FCC reflection groups with respect to temperature increase measured at three different heating rates. Note that the initially negative apparent lattice strain appearing in some of the reflection groups (e.g. 111, 220, and 311) is because of macroscopic compressive plastic deformation during cold rolling. Upon heating, reverse austenitic transformation, recovery, and thermal expansion can all take place. The lattice strains measured before the A_s temperature and after the A_f temperature are mostly due to recovery and thermal expansion. In between these two temperatures, reverse austenitic transformation takes place, and becomes the dominant factor for the lattice strain evolution. The following features are consistently observed in Fig. 5(a–c): (1) the highest and the lowest apparent lattice strains exist in the 200 and the 311 reflection groups throughout the entire heating period (25–500 °C); (2) the apparent lattice strain evolution firstly develops a linearly increasing trend as temperature increases. It is followed by evident inflections in 200, 222, and 311 reflection groups as the temperature falls in the range between A_s and A_f points. Upon the completion of the reverse austenitic transformation, all the apparent lattice strains develop subtle differences and again linearly increase as a function of temperature; and (3) the most salient apparent lattice strain inflection takes place in the 311 reflection groups in which a remarkable increase in the apparent lattice strain occurs at the upper vicinity of the A_s point.

The drastic uphill inflection of the 311 peak interestingly contradicts the volumetric contraction phenomena presumed for common martensite-to-austenite reverse transformation but indeed coincides with the classical dilatometer measurement of HCP-martensite, where an evident increase in the sample length is often associated with the onset of the transformation [51]. From a microscopic point of view, it can be explained by the actual unit cell size difference between FCC and HCP phases. As a first-order crystallographic approximation, the FCC and
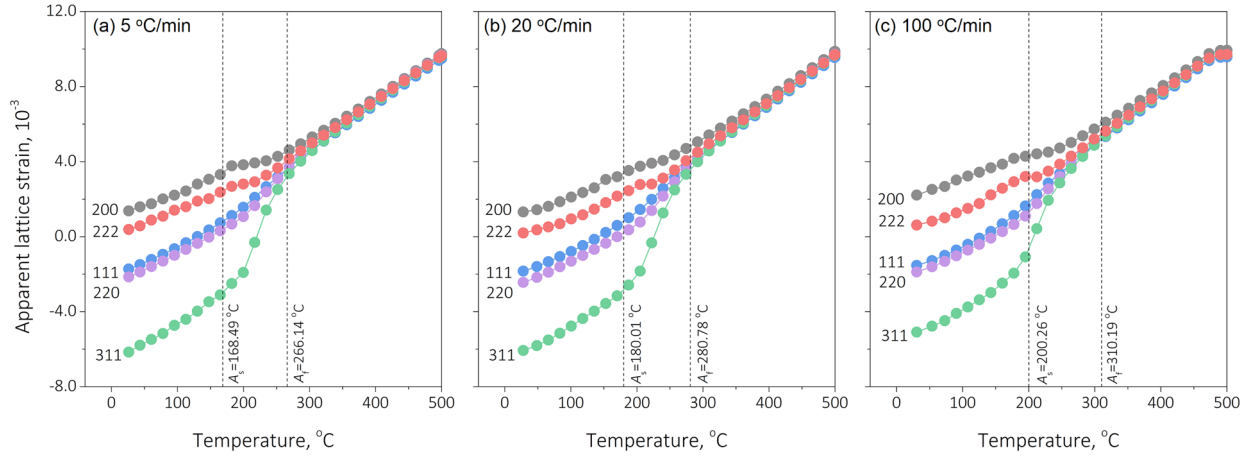
Figure 5: Apparent lattice strain evolution during reverse austenitic transformation under different heating rates: (a) 5 °C/min; (b) 20 °C/min; (c) 100 °C/min.

HCP unit size volumes, and the relative volumetric change can be respectively calculated as follows:

$$V_{FCC} = a_{FCC}^3 (4 - \text{atom reference unit cell}) \quad (6)$$

$$V_{HCP} = \frac{\sqrt{3}}{2} a_{HCP}^2 c_{HCP} (2 - \text{atom reference unit cell}) \quad (7)$$

$$\Delta V_{HCP-FCC} = \frac{V_{FCC} - 2V_{HCP}}{2V_{HCP}} \quad (8)$$

In Eqs. (6) and (7), a_{FCC}, a_{HCP}, and c_{HCP} are the parameters of the FCC and the HCP lattices. If taking the ambient temperature diffraction results in Fig. 5(a) as an exemplary calculation, $a_{FCC} = 3.601$ Å, $a_{HCP} = 2.537$ Å, and $c_{HCP} = 4.114$ Å, the corresponding $V_{FCC} = 46.693$ Å^3 and $V_{HCP} = 22.932$ Å^3. As a result, the relative volumetric difference achieves $+0.018$, indicating volumetric expansion during reverse austenitic transformation. Similar theoretical calculations are also carried out using the lattice parameters at higher temperatures (not shown here to avoid redundancy), and the same trend preserves. These results are consistent with our earlier investigation of the HCP-martensite in an FeMnCoCr quaternary alloy [52] and the systematic crystallographic study by Stanford et al. [53]

Another important feature embedded in Fig. 5(a–c) is the apparent lattice strain discrepancy between 111 and 222 reflection groups. Such a phenomenon has been well documented to be ascribed to the formation of intrinsic stacking faults [50, 54]. Because the apparent lattice strain calculated using Eq. (5) contains both elastic and inelastic portions:

$$\varepsilon_{hkl}^{app.} = \varepsilon_{hkl}^{sym.} - \frac{\sqrt{3}}{4\pi} \frac{\sum_b h + k + l}{(u+b)(h^2 + k^2 + l^2)} P_{sf} \quad (9)$$

The elastic part, $\varepsilon_{hkl}^{sym.}$ reveals a symmetric nature regardless of crystalline defects. The inelastic part, $\frac{\sqrt{3}}{4\pi} \frac{\sum_b h+k+l}{(u+b)(h^2+k^2+l^2)} P_{sf}$

is owing to the formation of intrinsic staking faults, in which u and b represent the number of unbroadened and broadened sub-reflection groups in the hkl diffraction signal. The term P_{sf}, stacking fault probability, directly quantifies the fraction of intrinsic stacking faults and can be calculated as follows:

$$P_{sf} = \frac{32\pi}{3\sqrt{3}} \left(\varepsilon_{222}^{app.} - \varepsilon_{111}^{app.} \right) \quad (10)$$

Figure 6(a1–a3) displays the stacking fault probability evolution under the three heating rates. Two kinetic stages can be visually identified: *first*, before the onset of reverse austenitic transformation, the P_{sf} value almost reveals a linear reduction from ~ 0.04 to ~ 0.035 as temperature increases; *second*, the P_{sf} largely follows an exponential decay during the transformation and this trend further extends, until the maximum temperature 500 °C is reached. The second kinetic stage is next quantitatively analyzed using an exponential decay function:

$$P_{sf} = A_0 \exp\left(-\frac{T}{\tau_0} \right) + K \quad (11)$$

Here, A_0 is a pre-factor that describes the amplitude of the decay, τ_0 is the decay constant which quantifies the rate of the decay, and K is the offset constant. In all three cases, good agreement with a correlation factor $R^2 > 0.99$ was achieved and the regression results are summarized in Table 2. It is seen that as the heating rate increases, A_0 reveals a monotonic increasing trend, implying the amplitude of P_{sf} decay increases. τ_0, on the other hand, demonstrates a monotonic decreasing trend, which suggests an increase in the decay rate. After the entire heating process, the P_{sf} values achieved through the three different heating rates are all ~ 0.0025 at 500 °C and reveal a subtle difference. The fact that P_{sf} does not eventually diminish plausibly suggests the absence of recrystallization or significant recovery. This can be interpreted as
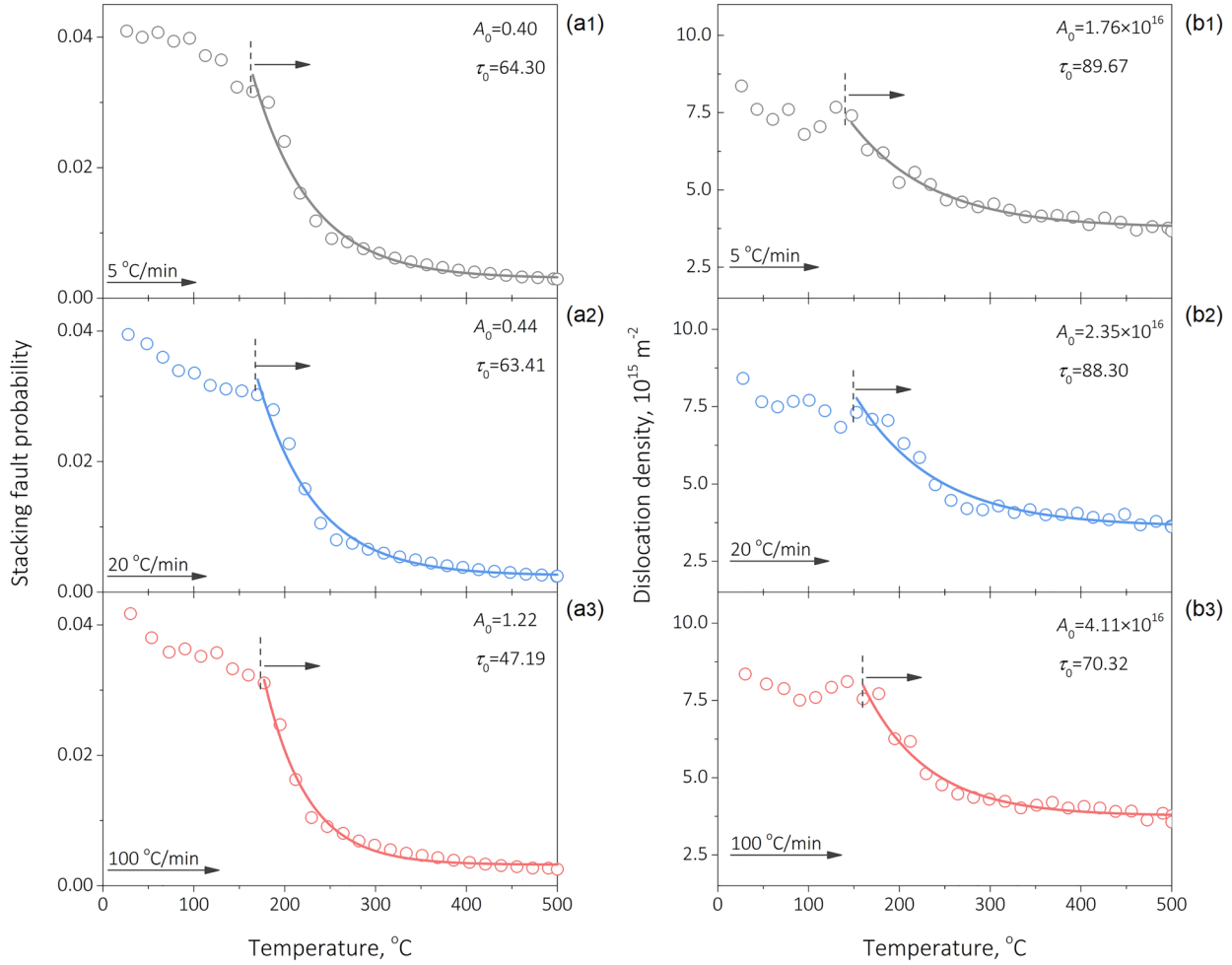
7

Figure 6: Stacking fault probability and dislocation density change during reverse austenitic transformation under different heating rates: (a1–a3) stacking fault probability evolution determined for three different heating rates; (b1–b3) dislocation density evolution calculated for three different heating rates.

TABLE 2: Kinetic quantification of the stacking fault probability and the dislocation density evolution.

Heating rate, °C/min	Stacking fault probability		Dislocation density	
	A_0	τ_0, °C	A_0, 10^{16} m^{-2}	τ_0, °C
5	0.40	64.30	1.76	89.67
20	0.44	63.41	2.35	88.30
100	1.22	47.19	4.11	70.32

follows: in a microstructural viewpoint, the FCC phase may still be defected and could contain some fractions of intrinsic stacking faults. The P_{sf} value of the HCP-phase may also be worth investigating; unfortunately, the crystallographic nature of the disordered HCP lattice hinders such analyses. In principle, determining P_{sf} for basal stacking faults in an HCP lattice requires the lattice strain values of both {0001} and {0002} reflection groups (similar with Eq. (10)). However, the extinction condition of a disordered HCP structure prevents the {0001} diffraction signal in synchrotron X-ray measurements. Since recent atomic resolution transmission electron microscopy study confirms the presence of basal faults in plastic strain-induced HCP-martensite [40], potential theoretical framework in quantifying P_{sf} using synchrotron X-ray data is, therefore, suggested for future work.

Resorting to the in situ diffraction results [Fig. 3(b1)], all FCC peaks exhibit some kinds of broadening at the ambient temperature after cold rolling [also see Fig. 1(c)], implying the significant involvement of (perfect) dislocations. Upon heating, however, such peak broadening trends attenuate. A widely accepted method to quantify dislocation density using diffraction data is the Williamson–Hall approach [55, 56], which states

$$\text{FWHM}\cos\theta_{hkl} = \frac{\lambda}{D} + \varepsilon_{micro}\sin\theta_{hkl} \qquad (12)$$

Here, FWHM, λ, ε_{micro}, D, and θ_{hkl} are the full width at half maximum of the diffraction peak, the wavelength of the X-ray beam (0.1173 Å in the present work), the micro-strain, the crystalline size, and the position of the hkl reflection group. The dislocation density can, therefore, be further determined using [55]

$$\rho = \frac{2\sqrt{3}\varepsilon_{micro}}{bD} \tag{13}$$

In Eq. (13), b is a normalization factor which takes the norm of the Burgers vector of the perfect dislocation in an FCC lattice, i.e. $b = \left|\frac{a}{2}[110]\right|$. In the current calculation, the influence of instrumental broadening (determined using the NIST standard CeO_2 powders) has been corrected [57]:

$$FWHM_{actual} = \left(FWHM_{apparent}^2 - FWHM_{instrument}^2\right)^{1/2} \tag{14}$$

The calculated dislocation density evolution trends are summarized in Fig. 6(b1–b3). Similar to the results on stacking fault probability, dislocation density under all three heating conditions also shows two kinetic evolution stages. Before the onset of the reverse austenitic transformation, the dislocation density shows a seemingly linear dependence with respect to the temperature increase. Upon the onset of the transformation and until 500 °C, the aforementioned exponential decay takes place, and the similar characteristics in A_0 and τ_0 evolution (see Table 2) is observed by regression analysis using Eq. (11). At the final stage of the experiment, a relatively higher dislocation density of 3.79×10^{15} m^{-2} was preserved in the 100 °C/min heating rate condition, compared with two other conditions. Since the major portions of the exponential decay functions Fig. 6 are within the $A_s - A_f$ temperature range (only the tail parts extend to higher temperatures), it is, therefore, suggestive that recovery plays a minor role in affecting the defect content compared with the reverse austenitic transformation. While the classical Williamson–Hall method used here quantifies the dislocation density, the properties and arrangements of these dislocations still require extensive future effort, for which physics-based models, such as the Warren–Averbach approach or its derivatives may be employed.

Considering the change in heating rate, the resultant differences in dislocation density and stacking fault probability among the three specimens are relatively small. Two core factors might play a role: *first,* the displacive nature of the HCP-FCC reverse transformation. Since the HCP-FCC reverse transformation accounts for the major activity during heating, a displacive mechanism (as detailed in the next section) tends to exhibit a relatively weak dependence of the onset temperature as a function of heating rate (Fig. 4). The total amounts of the defect being annihilated are, therefore, similar in all three conditions. *Second,* the highest temperature reached is not high enough to activate significant defect annihilation during recovery. After

the reverse austenitic transformation, all three specimens were only heated up to 500 °C. It can be expected that such a temperature is not sufficient to activate noticeable recovery given the three heating rates, and hence, the time scale of the measurements. Although the highest defect contents are achieved using the 100 °C/min heating rate, the differences among the three specimens are not significant.

Discussion

The displacive nature of reverse austenitic transformation

Quantitative assessments of the reverse austenitic transformation kinetics ("Kinetics of reverse austenitic transformation" section) underpin its displacive nature. The activation energy determined from the Kissinger-style analysis (171.38 kJ/mol), although consistently supporting a displacive mechanism, is slightly higher than the typical thermoelastic reverse austenitic transformation [47]. Such a discrepancy can be rationalized from the mechanical history of the martensite formation. Thermoelastic martensite mostly nucleates with the assistance of elastic stress, where martensitic transformation occurs before the yield point of the parent austenitic phase. Because of this, dislocation involvement in the parent phase is subtle, and as a result, the displacive reverse austenitic transformation takes place with rather moderate pre-existing dislocation–glissile interface interaction. In the case of the martensite induced by plastic straining, on the other hand, yielding of the parent phase is indispensable, which can lead to considerable dislocation formation. Upon heating, it can be anticipated that an additional energy barrier may exist due to the interface-dislocation interactions. In the present study, since the A_s temperature is ~ 168 °C [5 °C/min heating rate, Fig. 4(a1), for example], the decrease in dislocation density [Fig. 6(b1)] is proved to be subtle, an evident resistance of FCC/HCP interface movement can be, therefore, expected.

Atomistic mechanisms of the thermally-driven reverse austenitic transformation are conceived next, on the basis of the crystallographic theory for the FCC-HCP transformation [58]. During plastic deformation, the strain-induced HCP-martensite formation can be considered as a plasticity micro-mechanism that competes against perfect dislocation glide. The transformation takes place in such a way that the Shockley partial dislocations glide through every other {111}$_{FCC}$ plane. Figure 7(a1 and a4) depicts such a process with the partial Shockley partial dislocations denoted as b_p. Theoretically, the FCC/HCP interface exhibits a fully coherent structure, since the foregoing atomistic pathway enables an invariant plane strain, leaving {111}$_{FCC}$ undistorted [Fig. 7(a4)]. Because of this, the FCC/HCP interface can remain rather mobile. Upon thermal activation, the emitted Shockley partial dislocations may be able to glide
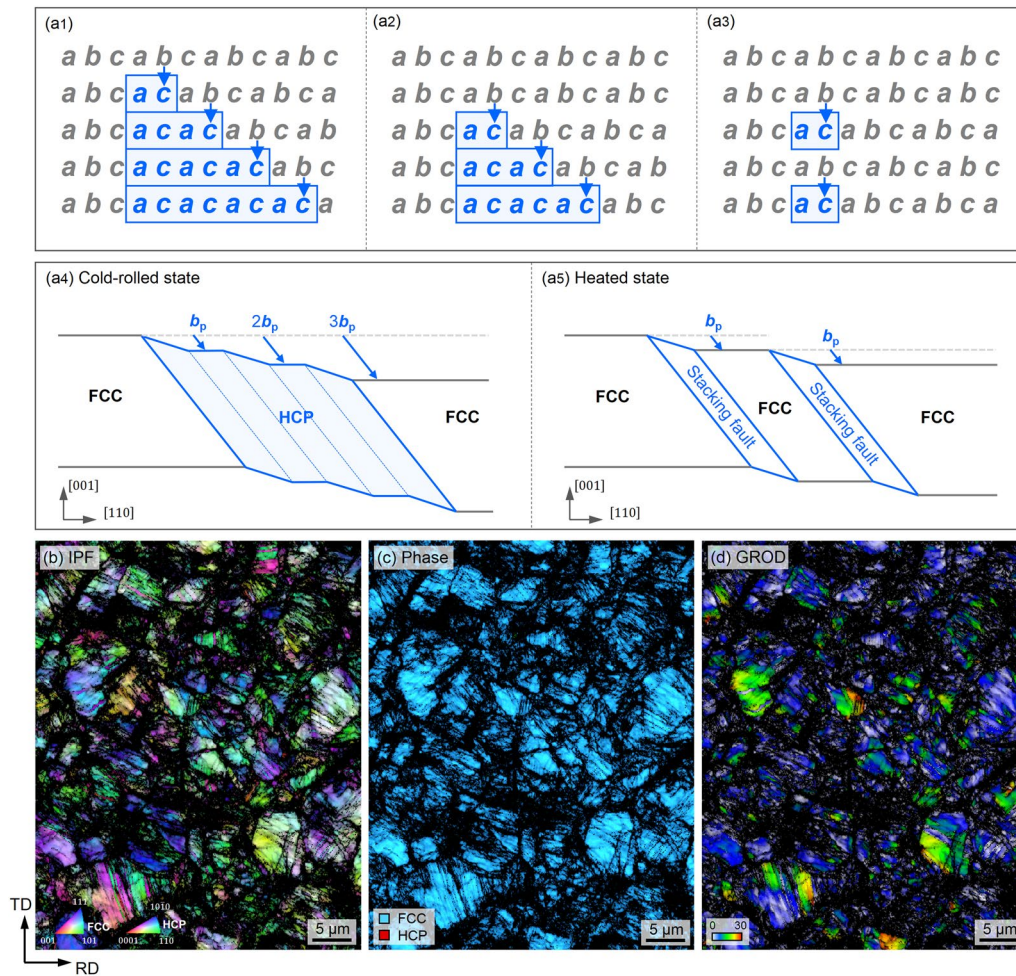
Figure 7: Atomistic mechanisms of displacive reverse austenitic transformation and the resulting microstructure: (a1–a3) sketches of the conceived atomistic pathway for the transformations (dislocations are not shown for clarity); (b) inverse pole figure; (c) phase map; (d) grain reference orientation deviation map. The EBSD measurements were obtained from the specimen subjected to 5 °C/ min heating rate, which presumably exhibits the highest recrystallization tendency.

following the previous pathway in reverse, enabling the reverse austenitic transformation [Fig. 7(a2)]. The conceived mechanisms are consistent with a recent in situ study on a metastable Fe–15Mn–10Cr–8Ni alloy [59], in which the reverse transformation of the HCP-martensite replicates the forward transformation pathway.

In reality, however, such a reverse transformation may also be accompanied by the formation of other types of crystalline defects. The most plausible defect category is intrinsic stacking faults, since the quantitative results shown in Fig. 6(a1–a3) supports their presence throughout the entire transformation process. This can be explained by the fact that due to the resistance from the pre-existing dislocations, the reverse glide of the Shockley partial dislocations may not be fully complete. Figure 7(a3) sketches such a possibility. Here, except the second and the fourth layers, all other Shockley partial dislocations manage to accomplish the reverse glide, which results in two incorrectly stacked FCC layers with an individual shear offset of b_p, i.e. the

intrinsic stacking faults [also see Fig. 7(a5)]. An earlier in situ transformation electron microscopy study of Fe–Mn-based metastable alloys supports these proposed mechanisms [60]: at an annealing temperature of 600 °C, massive stacking faults were observed along the FCC/HCP lamellar plates. Depending on the composition, however, detailed dislocation substructures inherited from such a reverse transformation pathway may strongly depend on the maximum temperature reached. Future in situ transmission electron microscopy studies are needed to unambiguously resolve the properties of these transformation-induced dislocations.

Since recrystallization is absent in all three heating conditions adopted in the present study, the FCC phase after reverse austenitic transformation should intrinsically be defected. Such a hypothesis is not only supported by the extensive dislocation density (at the 10^{15} m^{-2} order of magnitude) calculated in Fig. 6(b1–b3) but also further validated by the EBSD measurements in Fig. 7(b–d). Both the inverse pole figure (acquired along

the rolling direction, RD) and the phase map cross-confirm that the microstructure fully consists of FCC phase. The reduced image quality spanning over the entire regions in these two figures implies the extensive defect content, which coincides with the literature [29]. For better quantification, the grain reference orientation deviation (GROD) map is calculated and revealed in Fig. 7(d). The GROD value is in general high throughout the microstructure, confirming the presence of significant lattice distortion and thereby the high defect content [61]. It is worthwhile noting that some portions of the microstructure exhibit particularly higher GROD values than their vicinity. Although more dedicated efforts are deemed necessary to mechanistically consolidate this phenomenon, a plausible explanation may still be hypothesized considering plastic inhomogeneity during cold rolling. The 50 % thickness reduction introduced to the specimen can cause highly inhomogeneous plastic strain distribution throughout the microstructure. The dislocation density is, therefore, spatially non-uniform and much higher in some local regions. Upon heating up to 500 °C, although reverse austenitic transformation manages to complete in these regions because of thermodynamics, the high dislocation density due to heterogeneous local deformation is inherited, causing the much higher GROD values. It is also worth mentioning that since stacking faults exhibit elastic strain fields only around the vicinity of the partial dislocations, residual perfect dislocation density plays the more predominant role in affecting the GROD values.

Mechanical responses and insights into microstructural design

The final discussion point aims to explore the possibility in exploiting the foregoing displacive reverse austenitic transformation in microstructural design. To this end, the Vickers hardness values of the specimens after in situ synchrotron X-ray measurements were tested. As demonstrated in Fig. 8(a), under all three heating rates, the Vickers hardness values exceed 360 HV_{100gf}, indicating promising mechanical strength has been achieved after reverse austenitic transformation. The hardness value also exhibits a monotonic increasing trend as a function of heating rate. At the highest heating rate of 100 °C/min, a Vickers hardness value of 385.4 ± 2.19 HV_{100gf} is reached. Such a trend has two mechanistic implications: *first*, the increase of heating rate promotes the yield strength; and *second*, strain hardenability increases as the adopted heating rate elevates. The first hypothesis can be semi-quantitatively explained by the dislocation density results presented in Fig. 6(b1–b3). Upon the completion of the experiment, the highest dislocation density exists in the specimen tested under 100 °C/min heating rate, reaching 3.79×10^{15} m^{-2} (in comparison, 3.59×10^{15} m^{-2} for the 5 °C/min sample). As implied by the Taylor's equation [62] on the scaling relation between dislocation density and strength contribution, i.e. $\Delta\sigma \sim \sqrt{\rho_{disloc.}}$, the highest hardness in the specimen tested under 100 °C/min can be anticipated. In addition, the differences in stacking fault contents after cooling can also play a role. Supplementary Fig. S4 reveals the diffraction patterns and the corresponding P_{sf} values for all three samples cooled down to room temperature. A discernable increase in P_{sf} can be seen as heating rate increases, which also promotes the yield strength. Although future work is needed to fully elucidate the complex interplay between dislocations and stacking faults (especially when temperature changes), it can be hypothesized that the higher dislocation density can more effectively resist the shrinkage of stacking faults, leading to the higher P_{sf} values at the higher heating rates.
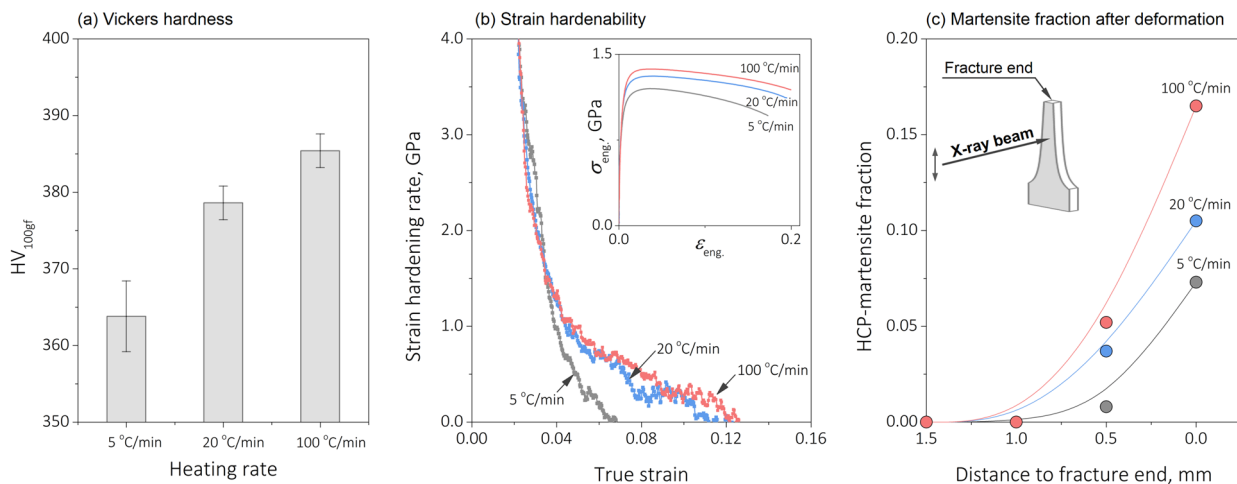

Figure 8: Mechanical responses of the specimens tested under different heating rates: (a) Vickers hardness; (b) strain hardening rate; and (c) HCP-martensite fraction with respect to the distance to fracture end. The inset of (b) shows the engineering stress–strain curves measured from the sub-standard specimens.

The second proposition on strain hardenability is more intriguing to be further examined, since apparent brittleness is often associated with highly defected microstructures [28, 63]. Because of the small dimensions of the in situ synchrotron X-ray specimens, only sub-standard tensile samples can be prepared. Details of the sample geometry are provided in Supplementary Fig. S5. Note that because of the well-documented sample size effect on tensile properties [64], the results reported here should not be utilized to evaluate the load-bearing performance or be compared with the literature data to highlight strength–ductility synergy. Instead, these tests were conducted just to enable more quantitative comparisons of the strain-hardening response. The measured strain-hardening rates for the three samples are demonstrated in Fig. 8(b). No evident brittleness exists in any of the tested samples (see the inset of Fig. 8(b) and fractography analyses in Supplementary Fig. S6). The yield points demonstrate increasing trends as the heating rate elevates, which is consistent with the Vickers hardness. Interestingly, the most evident drop in strain-hardening rate exists in the specimen measured under 5 °C/min heating rate. In contrast, the two other samples tested using higher heating rates (20 and 100 °C/min) demonstrate better strain hardenability. Such an increased strain hardenability may be explained by the higher strain-induced martensitic transformation potency. Figure 8(c) reveals the HCP-martensite fraction measured at different locations on the fractured tensile specimens using synchrotron X-ray. All three specimens demonstrate increasing HCP-martensite fractions as a function of decreasing distance to the fracture end. The HCP-martensite fraction in the specimen measured under 100 °C/min heating rate shows the highest value at all measured positions, which is consistent with the higher strain hardenability seen in Fig. 8(b). It can be hypothesized that the higher content of stacking faults within the specimen measured under 100 °C/min heating rate [Fig. 6(a3) and Supplementary Fig. S4] provides more nucleation sites for the HCP-martensite and thereby facilitates the transformation. Furthermore, the microscopic strain localization mechanisms can also affect the strain hardenability in these highly defected microstructures, for which future study is still required.

The foregoing mechanical responses achieved under different heating rates further bring about the opportunity for mechanistically-driven microstructural design. One of the major challenges of mechanically metastable ferrous alloys lie in the drastic loss of strain hardenability after immense nucleation of the martensite upon plastic straining [50, 52]. In the case of HCP-martensite formation, specifically, this kind of issue is mostly because of the limited number of slip systems in the HCP lattice [62] and the grain boundary micro-cracking [52]. The reverse austenitic transformation may be conceived as a processing solution in addition to compositional design. In principle, rapid heat treatment or up-quenching either through laser annealing [19, 65] or high-frequency induction heating can be applied to the deformed specimen, realizing the HCP-martensite reverse transformation within a time scale of $10^1 \sim 10^2$ s. As suggested by both the hardness and the strain hardenability assessments in Fig. 8(a and b), the resulting microstructures are anticipated to offer sufficient mechanical strength while maintaining plastic deformability. Given this sort of processing-microstructure-property correlation, an in-operando treatment can be realized to further improve the fatigue or wear resistance of metastable ferrous alloys.

Conclusions

In summary, the present work systematically examined the reverse austenitic transformation in a metastable $(Fe_{60}Mn_{40})_{85}Co_{15}$ alloy, with emphases on the transformation kinetics, atomistic mechanisms, and defect content evolution. Through in situ synchrotron X-ray study coupled with post-mortem electron microscopy characterizations, the following conclusions are drawn:

(1) Reverse austenitic transformation of the plastic strain-induced HCP-martensite can take place in a relatively low-temperature range (160–300 °C) and in a short time scale. The transformation kinetics assessed at 5, 20, and 100 °C/min heating rates all exhibit good agreement with the Boltzmann sigmoidal model. Kissinger-style analyses were carried out and the activation energy was determined as 171.38 kJ/mol, suggesting the displacive nature of the transformation;

(2) Stacking fault probability and dislocation density evolution during the reverse austenitic transformation were quantitatively assessed using the synchrotron X-ray diffraction data. Both quantities exhibit two-stage evolution trends with respect to the temperature increase: linear dependence appears before the onset of the transformation, while during and after the completion of the transformation, both quantities reveal the exponential attenuation $Y \sim \exp(-T)$;

(3) A plausible atomistic pathway for the reverse austenitic transformation was conceived based on the crystallographic theory. Mechanical property assessments reveal that the highest Vickers hardness of 385.4 ± 2.19 HV$_{100gf}$ exists in the specimen tested under 100 °C/min heating rate. Provided the high dislocation density of the reverted FCC phase, sub-standard tensile tests underpin the absence of apparent brittleness and the occurrence of stable strain hardenability. The mechanistic insights reported in the present work also contribute to the engineering merit in designing in-operando processing methods for metastable ferrous alloys.

Materials and methods

Alloy fabrication

The alloy utilized in the present study is a ternary metastable $(Fe_{60}Mn_{40})_{85}Co_{15}$ alloy that exhibits plastic strain-induced FCC to HCP martensitic transformation. Details of the compositional design concepts have been reported elsewhere [40]. The alloy was produced by vacuum arc melting of Fe, Mn, and Co elements with purity higher than 99.9 % using an Edmund Bühler GmbH AM500 arc melter. The specimen was melted, flipped, and re-melted for at least five times to avoid macroscopic segregation before suction cast into a rectangular ingot. The as-cast ingot was firstly cold rolled to 50 % thickness reduction and sealed in a quartz ampoule before homogenized at 1000 °C for 5 h. Upon the completion of the homogenization treatment, the ampoule was manually broken and the sample was quenched into ice water. This as-homogenized sample was further sectioned into several smaller pieces by wire electrical discharge machining (EDM). These smaller pieces were next cold rolled again to 50 % thickness reduction prepared for further experiments. One common issue during Mn-containing alloy processing is the inevitable Mn loss due to evaporation and oxidation [66, 67]. In the present study, energy-dispersive X-ray spectroscopy was utilized to semi-quantitatively assess the actual composition. The contents of Fe, Mn, and Co are 50.88 ± 0.88, 33.62 ± 0.53, and 15.50 ± 0.37 at.%, which are all consistent with the targeted values.

Microstructural analyses and mechanical property testing

Microstructural characterizations including, secondary electron (SE) imaging, backscatter electron imaging (BSE), electron channeling contrast imaging (ECCI), and energy-dispersive X-ray spectroscopy (EDS) were all carried out on a Tescan Mira 3 scanning electron microscope (SEM). Electron backscatter diffraction (EBSD) measurements were conducted using an EDAX Hikari camera at a working distance of ~18.00 mm with a 20 keV acceleration voltage. The EBSD data were further processed in an Orientation Imaging Microscopy (OIM) software to obtain quantitative crystallographic information. Specimens for these microstructural studies were prepared following the conventional metallographic sample preparation procedures. They were first mechanically ground on a series of SiC abrasive papers up to #800 grit then polished using 9, 3, 1 μm diamond suspension. The mirror-finished samples were eventually fine polished using colloid silica with ~40 nm diameters. To avoid surface etching or pitting corrosion, the PH level of the colloid silica was adjusted to neutral.

To assess the mechanical properties of the samples after reverse austenitic transformation achieved under different conditions, two types of mechanical tests were carried out. *First,*

Vickers hardness measurements: In these tests, the samples after in situ synchrotron X-ray experiments were utilized, and the preparation approaches have been provided above. 100 g force along with 15 s dwell time was adopted for the tests. To ensure statistical reliability, 7 measurements were performed on each sample, in which 5 datum points were averaged, excluding the maximum and the minimum values. *Second, sub-standard tensile tests:* Because of the geometric limitation of the in situ heating specimens (see details in the next section), only sub-standard tensile specimens can be utilized. These specimens with gauge dimensions of 1.8 mm × 1.2 mm × 1.0 mm were cut from the disks after in situ synchrotron X-ray measurements. Graphical sketches of them are provided in Supplementary Fig. S5 as a guide to the eye. Considering the well-documented size effects on tensile properties [64], it should be highlighted that the results reported in the present study can neither be utilized to quantify the load-bearing performance nor be compared with the literature data on strength-ductility synergies. Instead, these measurements were aimed at comparing the initial strain hardenability among different samples. These limitations have also been noted in the main text to avoid technical ambiguity and confusion. Uniaxial tensile tests were carried out using a Gatan micro-mechanical testing equipment. Following the previous experimental methods [68], the rectangular dog bone samples were speckle patterned for digital imaging correlation (DIC) analyses. During each uniaxial tensile measurement, optical images were taken every 0.5 s and were post-analyzed in a GOM correlate software (https://www.gom.com/3d-software/gom-correlate.html) to obtain engineering strain. The spatial resolution of these optical DIC measurements is ~140 pixel/mm. Square facet size and inter-facet distance employed in the strain calculation are ~0.14 mm (20 pixel) and ~0.07 mm (10 pixel). These parameters have been validated not to cause any artifacts in strain calculations.

In situ synchrotron X-ray measurements

Controlled heating rate tests were utilized to assess the reverse austenitic transformation mechanisms under synchrotron X-ray diffraction on Beamline 11 ID-C Argonne National Laboratory, Chicago, U.S.A. Disk-shaped samples with 6.5 mm diameters and 1.1 mm thicknesses were sectioned from the alloy sheet after 50 % cold rolling. Three heating rates, 5, 20, and 100 °C/min were chosen in the present work and were achieved on a Linkam THMS600 heating instrument (under Ar protection). During the heating process, a high-energy transmission X-ray beam with 0.1173 Å wavelength was shed on the sample to collect two-dimensional diffractograms at a working distance of ~1580 mm with an exposure time of 10 s. These parameters were chosen as they satisfactorily balance the spatial resolution and the number of diffraction peaks that can

be captured. A sketch of the experimental setup can be found in main text Fig. 2 and the actual configuration was included in Supplementary Fig. S2. Note that because the temperature will continuously increase during diffractogram aquisition, the temperature representation in the main text is an average of the temperatures when the shutter is open and close, i.e. $T = 1/2\left(T_{shutter\ open} + T_{shutter\ close}\right)$. Before quantitative diffraction analyses, the instrumental parameters were calibrated using the diffraction patterns of NIST standard CeO_2 powders. All recorded two-dimensional diffractograms were Rietveld refined in GSAS-II software [69] coupled with home-built MATLAB programs for peak position, dislocation density, and stacking fault probability calculations. A residual error $R_{wp} < 8.0\ \%$ was ensured in each Rietveld refinement. Different from the case in any uniaxial tensile test, the anisotropy in lattice strain along the transverse and the rolling directions is subtle. The sanity check is provided in Supplementary Fig. S7 where the lattice strains are calculated using transverse direction, rolling direction, and overall integrations.

Acknowledgments

Author contributions

SLW: conceptualization, experimental investigations, programing, theoretical calculations, formal analysis, and writing – original draft. JK: experimental investigations and discussion; CCT: conceptualization, formal analysis, writing – review and editing, project coordination, and supervision. All authors discussed and approved the final version of the manuscript.

Funding

Data availability

The data that support the findings of this study are available from the corresponding author (tasan@mit.edu) upon reasonable request.

Declarations

Conflict of interest The authors declare that they have no known competing financial interests or personal relationships that could have appeared to influence the work reported in this manuscript.

Supplementary Information

The online version contains supplementary material available at https://doi.org/10.1557/s43578-022-00818-5.

Open Access

References

1. A.L. Roitburd, G.V. Kurdjumov, Mater. Sci. Eng. **39**, 141 (1979)

2. M. Bouville, R. Ahluwalia, Interplay between diffusive and displacive phase transformations: time-temperature-transformation diagrams and microstructures. Phys. Rev. Lett. **97**(5), 055701 (2006)

3. E.M. Mazzer, M.R. da Silva, P. Gargarella, J. Mater. Res. **37**, 162 (2022)

4. G.B. Olson, M. Cohen, A mechanism for the strain-induced nucleation of martensitic transformations. J. Less-Common Met. **28**(1), 107 (1972)

5. J.R. Patel, M. Cohen, Criterion for the action of applied stress in the martensitic transformation. Acta Metall. **1**(5), 531 (1953)

6. U. Kühn, J. Romberg, N. Mattern, H. Wendrock, J. Eckert, Transformation-induced plasticity in Fe–Cr–V–C. J. Mater. Res. **25**, 368 (2010)

7. H. Zhang, M. Sun, Y. Liu, D. Ma, B. Xu, M. Huang, D. Li, Y. Li, Ultrafine-grained dual-phase maraging steel with high strength and excellent cryogenic toughness. Acta Mater. **211**, 116878 (2021)

8. N. Tsuchida, T. Tanaka, Y. Toji, Effect of deformation temperature on mechanical properties in 1-gpa-grade trip steels with different retained austenite morphologies. ISIJ Int. **61**(2), 564 (2021)

9. X.S. Yang, S. Sun, H.H. Ruan, S.Q. Shi, T.Y. Zhang, Shear and shuffling accomplishing polymorphic fcc γ → hcp ε → bct α martensitic phase transformation. Acta Mater. **136**, 347 (2017)

10. J.W. Christian, Analyses of lattice and shape deformations and of atomic shuffles in martensitic transformation. Mater. Sci. Eng. A **127**(2), 215 (1990)

11. S. Wei, J. Kim, J.L. Cann, R. Gholizadeh, N. Tsuji, C.C. Tasan, Plastic strain-induced sequential martensitic transformation. Scr. Mater. **185**, 36 (2020)

12. M. Soleimani, A. Kalhor, H. Mirzadeh, Transformation-induced plasticity (TRIP) in advanced steels: a review. Mater. Sci. Eng. A **795**, 140023 (2020)

13. K. Yamanaka, M. Mori, Y. Koizumi, A. Chiba, Local strain evolution due to athermal γ→ε martensitic transformation in biomedical CoCrMo alloys. J. Mech. Behav. Biomed. Mater. **32**, 52 (2014)

14. S. Wei, F. He, C.C. Tasan, Metastability in high-entropy alloys: a review. J. Mater. Res. **33**(19), 2924 (2018)

15. J. Langner, J.R. Cahoon, Increase in the alpha to gamma transformation temperature of pure iron upon very rapid heating. Metall. Mater. Trans. A Phys. Metall. Mater. Sci. **41**, 1276 (2010)

16. L. Xue, K.C. Atli, S. Picak, C. Zhang, B. Zhang, A. Elwany, R. Arroyave, I. Karaman, Controlling martensitic transformation characteristics in defect-free NiTi shape memory alloys fabricated using laser powder bed fusion and a process optimization framework. Acta Mater. **215**, 117017 (2021)

17. Y.Y. Meshkov, E.V. Pereloma, Phase Transformations in Steels, Vol 1 in Woodhead Publishing Series in Metals and Surface Engineering, 2012, p. 581–618. https://www.sciencedirect.com/science/article/pii/B9781845699703500179

18. R. Neugebauer, S. Scheffler, R. Poprawe, A. Weisheit, Local laser heat treatment of ultra high strength steels to improve formability. Prod. Eng. **3**(4–5), 347 (2009)

19. P. Lapouge, J. Dirrenberger, F. Coste, M. Schneider, Laser heat treatment of martensitic steel and dual-phase steel with high martensite content. Mater. Sci. Eng. A **752**, 128 (2019)

20. M. Asadi, G. Frommeyer, A. Aghajani, I. Timokhina, H. Palkowski, Local laser heat treatment in dual-phase steels. Metall. Mater. Trans. A Phys. Metall. Mater. Sci. **43**(4), 1244 (2012)

21. P. Kürnsteiner, M.B. Wilms, A. Weisheit, P. Barriobero-Vila, E.A. Jägle, D. Raabe, Massive nanoprecipitation in an Fe-19Ni-xAl maraging steel triggered by the intrinsic heat treatment during laser metal deposition. Acta Mater. **129**, 52 (2017)

22. S. Amirabdollahian, F. Deirmina, L. Harris, R. Siriki, M. Pellizzari, P. Bosetti, A. Molinari, Towards controlling intrinsic heat treatment of maraging steel during laser directed energy deposition. Scr. Mater. **201**, 113973 (2021)

23. Y. Yin, Q. Tan, M. Bermingham, N. Mo, J. Zhang, M.X. Zhang, Laser additive manufacturing of steels. Int. Mater. Rev. **67**(5), 487 (2022)

24. Y.K. Lee, J. Han, Current opinion in medium maganese steel. Mater. Sci. Technol. **31**, 843 (2015)

25. E. Dryzek, M. Sarnek, M. Wróbel, Reverse transformation of deformation-induced martensite in austenitic stainless steel studied by positron annihilation. J. Mater. Sci. **49**(24), 8449 (2014)

26. J. Han, Y.K. Lee, The effects of the heating rate on the reverse transformation mechanism and the phase stability of reverted austenite in medium Mn steels. Acta Mater. **67**, 354 (2014)

27. A.S. Hamada, A.P. Kisko, P. Sahu, L.P. Karjalainen, Enhancement of mechanical properties of a TRIP-aided austenitic stainless steel by controlled reversion annealing. Mater. Sci. Eng. A **628**, 154 (2015)

28. D. Raabe, S. Sandlöbes, J. Millán, D. Ponge, H. Assadi, M. Herbig, P.P. Choi, Segregation engineering enables nanoscale martensite to austenite phase transformation at grain boundaries: a pathway to ductile martensite. Acta Mater. **61**(16), 6132 (2013)

29. Y. Lü, B. Hutchinson, D.A. Molodov, G. Gottstein, Effect of deformation and annealing on the formation and reversion of ε-martensite in an Fe–Mn–C alloy. Acta Mater. **58**(8), 3079 (2010)

30. C. Haase, M. Kühbach, L.A. Barrales-Mora, S.L. Wong, F. Roters, D.A. Molodov, G. Gottstein, Recrystallization behavior of a high-manganese steel: experiments and simulations. Acta Mater. **100**, 155 (2015)

31. Y. Lü, D.A. Molodov, G. Gottstein, Recrystallization kinetics and microstructure evolution during annealing of a cold-rolled Fe–Mn–C alloy. Acta Mater. **59**(8), 3229 (2011)

32. C. Haase, S.G. Chowdhury, L.A. Barrales-Mora, D.A. Molodov, G. Gottstein, On the relation of microstructure and texture evolution in an austenitic Fe-28Mn-0.28C TWIP steel during cold rolling. Metall. Mater. Trans. A Phys. Metall. Mater. Sci. **44**(2), 911 (2013)

33. F. Berrenberg, C. Haase, L.A. Barrales-Mora, D.A. Molodov, Enhancement of the strength-ductility combination of twinning-induced/transformation-induced plasticity steels by reversion annealing. Mater. Sci. Eng. A **681**, 56 (2017)

34. S. Pramanik, A.A. Saleh, E.V. Pereloma, A.A. Gazder, Effect of isochronal annealing on the microstructure, texture and mechanical properties of a cold-rolled high manganese steel. Mater. Charact. **144**, 66 (2018)

35. F. Brasche, C. Haase, L.A. Barrales-Mora, D.A. Molodov, Comparative study of the influence of reversion- and recovery-annealing on the mechanical behavior of high-manganese steels with varying stacking fault energy. Steel Res. Int. **89**(9), 1700377 (2018)

36. T. Gebhardt, D. Music, B. Hallstedt, M. Ekholm, I.A. Abrikosov, L. Vitos, J.M. Schneider, Ab initio lattice stability of fcc and hcp Fe–Mn random alloys. J. Phys. Condens. Matter **22**(29), 295402 (2010)

37. T. Tsumuraya, I. Watanabe, T. Sawaguchi, Origin of phase stability in Fe with long-period stacking order as an intermediate phase in cyclic γ-ε Martensitic transformation. Phys. Rev. Res. **3**(3), 033215 (2021)

38. V.A. Esin, R. Mallick, M. Dadé, B. Denand, J. Delfosse, P. Sallot, Combined synchrotron X-ray diffraction, dilatometry and

electrical resistivity in situ study of phase transformations in a Ti₂AlNb alloy. Mater. Charact. **169**, 110654 (2020)

39. J.D. Escobar, G.A. Faria, L. Wu, J.P. Oliveira, P.R. Mei, A.J. Ramirez, Austenite reversion kinetics and stability during tempering of a Ti-stabilized supermartensitic stainless steel: correlative in situ synchrotron x-ray diffraction and dilatometry. Acta Mater. **138**, 92 (2017)

40. S. Wei, M. Xu, J.M. LeBeau, C.C. Tasan, Tuning mechanical metastability in FeMnCo medium entropy alloys and a peek into deformable hexagonal close-packed martensite. Appl. Phys. Lett. **119**(26), 261905 (2021)

41. Y. Tomota, M. Strum, J.W. Morris, Microstructural dependence of Fe-high Mn tensile behavior. Metall. Trans. A **17**(3), 537 (1986)

42. Y.K. Lee, C.S. Choi, Driving force for γ → ε martensitic transformation and stacking fault energy of γ in Fe–Mn binary system. Metall. Mater. Trans. A Phys. Metall. Mater. Sci. **31**(2), 355 (2000)

43. M. Acet, T. Schneider, B. Gehrmann, E.F. Wassermann, The magnetic aspects of the γ-α and γ-ε martensitic transformations in Fe–Mn alloys. Le J. Phys. IV **5**(C8), C8 (1995)

44. H.E. Kissinger, Reaction kinetics in differential thermal analysis. Anal. Chem. **29**(11), 1702 (1957)

45. R.T. Yang, M. Steinberg, Reaction kinetics and differential thermal analysis. J. Phys. Chem. **80**(9), 965 (1976)

46. N. Jetta, N. Ozdemir, S. Rios, D. Bufford, I. Karaman, X. Zhang, Phase transformations in sputtered Ni–Mn–Ga magnetic shape memory alloy thin films. Thin Solid Films **520**(9), 3433 (2012)

47. Z.N. Zhou, L. Yang, R.C. Li, J. Li, Q.D. Hu, J.G. Li, Martensitic transformations and kinetics in Ni–Mn–In–Mg shape memory alloys. Intermetallics **92**, 49 (2018)

48. W. Assassa, P. Guiraldenq, Bulk and grain boundary diffusion of 59Fe, 51Cr, and 63Ni in austenitic stainless steel under influence of silicon content. Met. Sci. **12**(3), 123 (1978)

49. L. Huang, W. Lin, K. Wang, S. Song, C. Guo, Y. Chen, Y. Li, F. Liu, Grain boundary-constrained reverse austenite transformation in nanostructured Fe alloy: model and application. Acta Mater. **154**, 56 (2018)

50. S. Wei, C.C. Tasan, Deformation faulting in a metastable CoCrNiW complex concentrated alloy: a case of negative intrinsic stacking fault energy? Acta Mater. **200**, 922 (2020)

51. L.M. Guerrero, P. La Roca, F. Malamud, A. Baruj, M. Sade, Experimental determination of the driving force of the fcc-hcp martensitic transformation and the stacking fault energy in high-Mn Fe–Mn–Cr steels. J. Alloys Compd. **797**, 237 (2019)

52. S. Wei, J. Kim, C.C. Tasan, Boundary micro-cracking in metastable Fe₄₅Mn₃₅Co₁₀Cr₁₀ high-entropy alloys. Acta Mater. **168**, 76 (2019)

53. N. Stanford, D.P. Dunne, Effect of Si on the reversibility of stress-induced martensite in Fe–Mn–Si shape memory alloys. Acta Mater. **58**, 6752 (2010)

54. R.P. Reed, R.E. Schramm, Relationship between stacking-fault energy and x-ray measurements of stacking-fault probability and microstrain. J. Appl. Phys. **45**, 4705 (1974)

55. G.K. Williamson, R.E. Smallman, The use of Fourier analysis in the interpretation of X-ray line broadening from cold-worked iron and molybdenum. Acta Crystallogr. **7**(8), 574 (1954)

56. R.E. Smallman, K.H. Westmacott, Stacking faults in face-centred cubic metals and alloys. Philos. Mag. **2**(17), 669 (1957)

57. J. Wang, L. Wang, G. Zhu, B. Zhou, T. Ying, X. Zhang, Q. Huang, Y. Shen, X. Zeng, H. Jiang, Understanding the high strength and good ductility in LPSO-containing Mg alloy using synchrotron X-ray diffraction. Metall. Mater. Trans. A Phys. Metall. Mater. Sci. **49**(11), 5382 (2018)

58. G.B. Olson, M. Cohen, A general mechanism of martensitic nucleation: part I. General concepts and the FCC → HCP transformation. Metall. Trans. A **7**, 1897 (1976)

59. M. Koyama, M. Seo, K. Nakafuji, K. Tsuzaki, Stacking fault aggregation during cooling composing FCC–HCP martensitic transformation revealed by in-situ electron channeling contrast imaging in an Fe-high Mn alloy. Sci. Technol. Adv. Mater. **22**(1), 135 (2021)

60. Y. Tomota, Y. Morioka, W. Nakagawara, Epsilon martensite to austenite reversion and related phenomena in Fe-24Mn and Fe-24Mn-6Si alloys. Acta Mater. **46**(4), 1419 (1998)

61. S.-S. Rui, L.-S. Niu, H.-J. Shi, S. Wei, C.C. Tasan, Diffraction-based misorientation mapping: a continuum mechanics description. J. Mech. Phys. Solids **133**, 103709 (2019)

62. P. M. Anderson, J. P. Hirth, and J. Lothe, Theory of dislocations 3rd Edition, 2017, Cambridge University Press

63. H. K. D. H. Bhadeshia, Theory of transformations in steels, 2021, CRC Press

64. Y.H. Zhao, Y.Z. Guo, Q. Wei, T.D. Topping, A.M. Dangelewicz, Y.T. Zhu, T.G. Langdon, E.J. Lavernia, Influence of specimen dimensions and strain measurement methods on tensile stress-strain curves. Mater. Sci. Eng. A **525**(1–2), 68 (2009)

65. S. Sanzaro, C. Bongiorno, P. Badalà, A. Bassi, G. Franco, P. Vasquez, A. Alberti, A. La Magna, Inter-diffusion, melting and reaction interplay in Ni/4H-SiC under excimer laser annealing. Appl. Surf. Sci. **539**, 539 (2021)

66. M. Waldenström, An experimental study of carbide-austenite equilibria in iron- base alloys with Mo, Cr, Ni, and Mn in the temperature range 1173 to 1373 K. Metall. Trans. A **8**(12), 1963 (1977)

67. J. Chu, Y. Bao, Study on the relationship between vacuum denitrification and manganese evaporation behaviours of manganese steel melts. Vacuum **192**, 110420 (2021)

68. S. Wei, J. Kim, C.C. Tasan, In-situ investigation of plasticity in a Ti–Al–V–Fe (α+β) alloy: slip mechanisms, strain localization, and partitioning. Int. J. Plast. **148**, 103131 (2022)

69. B.H. Toby, R.B. Von Dreele, GSAS-II: the genesis of a modern open-source all purpose crystallography software package. J. Appl. Crystallogr. **46**, 544 (2013)

Publisher's Note Springer Nature remains neutral with regard to jurisdictional claims in published maps and institutional affiliations.